International Journal of Nanomedicine

Dovepress
open access to scientific and medical research

Open Access Full Text Article

ORIGINAL RESEARCH

The Therapeutic Effects of MUC1-C shRNA@Fe_3O_4 Magnetic Nanoparticles in Alternating Magnetic Fields on Triple-Negative Breast Cancer

Zhifeng Li[1,2], Ting Guo[3], Susu Zhao[4], Mei Lin[2]

[1]Medical School of Nantong University, Nantong, Jiangsu, People's Republic of China; [2]Clinical Laboratory, Taizhou People's Hospital (Affiliated Hospital 5 of Nantong University), Taizhou, Jiangsu, People's Republic of China; [3]Research Center of Clinical Medicine, Taizhou People's Hospital (Affiliated Hospital 5 of Nantong University), Taizhou, Jiangsu, People's Republic of China; [4]Department of Pathology, Affiliated Hospital of Nanjing University of Chinese Medicine, Nanjing, Jiangsu, People's Republic of China

Correspondence: Mei Lin, Tel +86-052389890037, Email trylm@ntu.edu.cn

Purpose: Improving the treatment of triple-negative breast cancer (TNBC) is a serious challenge today. The primary objective of this study was to construct MUC1-C shRNA@ Fe_3O_4 magnetic nanoparticles (MNPs) and investigate their potential therapeutic benefits in alternating magnetic fields (AMF) on TNBC.

Methods: Firstly, we verified the high expression of MUC1 in TNBC and synthesized specific MUC1-C shRNA plasmids (MUC1-C shRNA). Then, we prepared and characterized MUC1-C shRNA@Fe_3O_4 MNPs and confirmed their MUC1-C gene silencing effect and magneto-thermal conversion ability in AMF. Moreover, the inhibitory effects on TNBC in vitro and in vivo were observed as well as biosafety. Finally, the protein levels of BCL-2-associated X protein (Bax), cleaved-caspase3, glutathione peroxidase inhibitor 4 (GPX4), nuclear factor erythroid 2-related factor 2 (NRF2), and ferritin heavy chain 1 (FTH1) in TNBC cells and tissues were examined, and it was speculated that apoptosis and ferroptosis were involved in the synergistic treatment.

Results: MUC1-C shRNA@ Fe_3O_4 MNPs have a size of ~75 nm, with an encapsulation rate of (29.78±0.63) %, showing excellent gene therapy and magnetic hyperthermia functions. Under a constant AMF (3Kw) and a set concentration (200μg mL^{-1}), the nanoparticles could be rapidly warmed up within 20 minutes and stabilized at about 43 °C. It could be uptaken by TNBC cells through endocytosis and significantly inhibit their proliferation and migration, with a growth inhibition rate of 79.22% for TNBC tumors. After treatment, GPX4, NRF2, and FTH1 expression levels in TNBC cells and tumor tissues were suppressed, while Bax and cleaved-caspase3 were increased. As key therapeutic measures, gene therapy, and magnetic hyperthermia have shown a synergistic effect in this treatment strategy, with a combined index (q index) of 1.23.

Conclusion: In conclusion, we developed MUC1-C shRNA@Fe_3O_4 MNPs with magnetic hyperthermia and gene therapy functions, which have shown satisfactory therapeutic effects on TNBC without significant side effects. This study provides a potential option for the precision treatment of TNBC.

Keywords: triple-negative breast cancer, nanoparticle, MUC1, hyperthermia, ferroptosis

Introduction

Breast cancer (BC) is a malignant tumor originating from the epithelial tissue of the breast and is the most common malignancy in women.[1] It is estimated that by 2040, there will be 3,000,000 new cases of BC and 100,000 deaths worldwide. Triple-negative breast cancer (TNBC), which accounts for 15–20% of all types of BCs, is the most malignant type of BC and is identified by the lack of estrogen receptor (ER), progesterone receptor (PR), and human epidermal growth factor receptor 2 (HER-2).[2] To date, due to the lack of molecular therapeutic targets, chemotherapy (paclitaxel-based, anthracyclines-based, and platinum-based et al) is still the mainstay of pharmacological treatment for patients with TNBC. However, the presence of TNBC is highly heterogeneous, it is susceptible to drug resistance, and the side effects of chemotherapeutic agents are often unacceptable In recent years, targeted, immunological, and antibody-drug conjugates (ADC) drugs have come on the scene, bringing hope for precision treatment of

Received: 27 July 2023
Accepted: 25 September 2023
Published: 6 October 2023

TNBC patients. For example, PARP inhibitors have been used to treat BRCA1/2-positive patients with advanced TNBC, and prolonged progression-free survival (PFS) and improved objective-response rate (ORR) have been observed.[3] Although the emergence of PARP inhibitors has broken the TNBC treatment landscape, the proportion of BRCA1/2 mutated TNBC patients is not high, and the prospect of their application remains to be explored. Theoretically, TNBC with a high tumor mutation load, a high proportion of tumor-infiltrating lymphocytes, and a high proportion of PD-L1-positive cells can benefit from immunotherapy. Studies have shown that early-stage PD-L1-positive TNBC patients can benefit from the treatment regimen of the immunological drug pembrolizumab combined with chemotherapy, but the results are poor for patients in advanced stages, thus immunotherapy has some limitations.[4,5] Next, ADC drugs are paid attention to, such as sacituzumab govitecan, which have achieved good efficacy in the treatment of TNBC by carrying specific antibodies on the chemotherapeutic agent SN-38 and precisely delivering highly toxic, high-dose chemotherapeutic agents to cancer cells through the target point of Trop-2.[6] However, their essence is still chemotherapeutic agents, and they are highly toxic, high-dose chemotherapeutic agents, with high side effects relative to conventional chemotherapy. The current low overall survival and poor prognosis of TNBC patients necessitate the identification of new molecular therapeutic targets and new therapeutic strategies to improve the efficacy of current anti-TNBC therapies and increase the patients' survival time.

Mucin 1 (MUC1) is a gene that contains 11 exons located on chromosome 1q22. After being translated into a polypeptide, MUC1 was auto-cleaved into two subunits: extracellular domain (ED, MUC1-N) and cytoplasmic domain (CD, MUC1-C), formed stable non-covalent heterodimeric complexes on the cell membrane and served as the boundary of the apical portion of normally polarized epithelial cells.[7] In normal breast tissue, MUC1-N forms a protein gel that acts as a physical barrier to protect mammary lining ducts; meanwhile, the cytoplasmic structure, MUC1-C, acts as a transmembrane receptor that transmits signals to the cell interior.[8]

In approximately 90% of TNBCs, MUC1 is abnormally amplificated and the self-transcriptional circuit is activated,[9,10] and the MUC1-N/MUC1-C complex is spread throughout the apical-basal polarity-deficient BC cell membranes. Due to the limitations in the understanding of MUC1 in the early days, the main focus was on the shed mucin subunit MUC1-N, and the representative was CA15-3, which has been one of the common cancer markers and follow-up indicators in clinical practice. However, because MUC1-N has a variable number of tandem repeats (VNTR), none of the therapeutic studies have achieved substantial results that can be used in clinic. Gradually, as the understanding of the structure and function of MIUC1 has deepened, researchers have found that MUC1-C plays a more important role in the occurrence and development of TNBC. MUC1-C can influence the progression of TNBC, but not limited to the following mechanisms (Scheme 1): 1. Activate the polybromo-1 (PBRM1), PRR/STING-mediated interferon (IFN) signaling pathway, inducing chronic inflammation and promoting cancer progression,[11–13] DNA damage resistance and immunosuppression;[14–16] 2. Interacts with EGFR, ErbB2, and other receptor tyrosine kinases on the cell membrane to activate the PI3K→AKT and MEK→ERK pathways; 3. Localizes to the nucleus and activates the WNT/β-linked protein, STAT, and NF-κB/RelA pathways;[17] 4. Enhances PD-L1 transcription by recruiting MYC and NF-κB p65 to the PD-L1 promoter, promoting immune escape of TNBC;[18] 5. Directly interact with MYC to activate the NuRD complex and mediate estrogen receptors in TNBC cell regulation.[19] In summary, MUC1-C induces the occurrence and development of TNBC by activating multiple signal pathways, reshaping chromatin structure, modifying epigenetic characteristics, and endowing TNBC with DNA damage resistance, drug resistance, stemness, and immune evasion ability.[20–22]

In conclusion, numerous evidences now suggest that MUC1-C is one of the potential therapeutic targets for TNBC. Therapies and strategies targeting MUC1-C for TNBC treatment were constantly being attempted. Some MUC1-C monoclonal antibodies or MUC1-C based TNBC therapies achieved promising results in laboratory, even some targeted anti-MUC1-C therapeutics have entered the phase II-III clinical trials.[8] However, unfortunately, almost all clinical trials failed to achieve the expected results, one important reason being the high heterogeneity of TNBC.[23] Therefore, combining treatment that can overcome tumor heterogeneity with MUC1-C gene therapy may be a potentially effective treatment strategy for TNBC.

It is well known that hyperthermia has the physical property that can directly lead to cell death, irrespective of cell heterogeneity. More subtly, loco-regional moderate hyperthermia (LRMH), which slightly increases the local temperature of the tumor to 39–44 °C and exposes cancer cells to supraphysiological temperatures,[24] can both directly cause cell death and modulate tumor immunity,[25] enhance the sensitivity of other treatment options such as radiotherapy and chemotherapy.[26,27] The idea of killing tumor cells by temperature can overcome heterogeneity and has been used in the field of BC treatment.[28] However, for solid tumors, including BC, the limited penetration of simple localized moderate

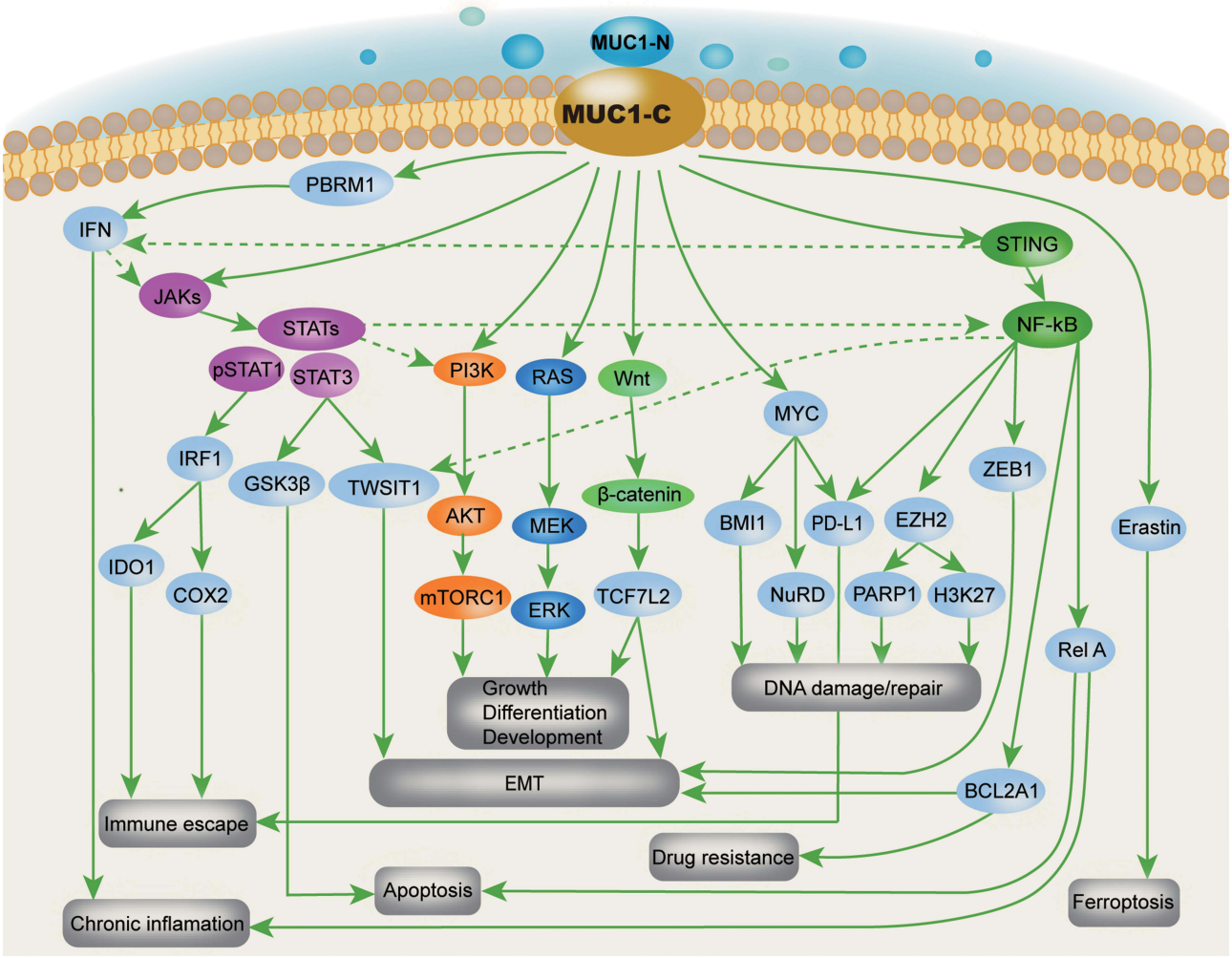

Scheme 1 Signal pathway and mechanism of MUC1-C regulating TNBC Occurrence and progression (Comprehensive arrangement according to the published articles).

heat therapy, and the long duration and treatment period of a single treatment session limit its application. Nevertheless, this does not prevent LRMH from being an ideal synergistic treatment.

With the development of nanotechnology, some nanoparticles have been shown to generate heat under the action of the magnetic field, laser, or ultrasound, which has a great potential to be used for tumor hyperthermia.[29] Since these nanoparticles are also able to carry gene-targeted drugs, chemotherapeutic drugs, etc, they can achieve the synergistic effect of multiple therapeutic methods simultaneously on a compound platform.[30] Hyperthermia combined with nanotechnology opened a new chapter for tumor treatment.[31,32] Of note, among those nanomaterials, Fe_3O_4 MNP is one of the most remarkable ones, which not only possesses some characteristics of ordinary nanomaterials such as bulk effect, surface effect, and quantum size effect, but also has good drug-carrying ability, biosafety, and magneto-thermal conversion ability. Fe_3O_4 MNP has been designed for the treatment of different types of cancers.[33] Theoretically, using Fe_3O_4 MNP as a carrier means it is possible to deliver gene drugs to the tumor cells; meanwhile, owing to its good magnetic thermal efficiency, it can also play a thermal therapeutic role in the AMF.

In the present research, we designed three MUC1-C shRNA plasmids (MUC1-C shRNA) and combined the most efficient one with Fe_3O_4 MNPs to establish a gene-hyperthermia therapeutic system. Firstly, the nanoparticles were characterized by DSL, TEM et al Then, the effects of MUC1-C shRNA@Fe_3O_4 MNPs (MUC1-C shRNA@Fe_3O_4) in AMF on TNBC were investigated in vitro and in vivo by examining cell migration, invasion, proliferation, tumor growth, and the expressions of the related genes, as well, the biosafety was evaluated.

Our study confirmed the efficacy and safety of MUC1-C shRNA@Fe_3O_4 MNPs in treating TNBC under AMF conditions. We cautiously propose that this may be a potential therapeutic method and strategy for TNBC treatment (Scheme 2).

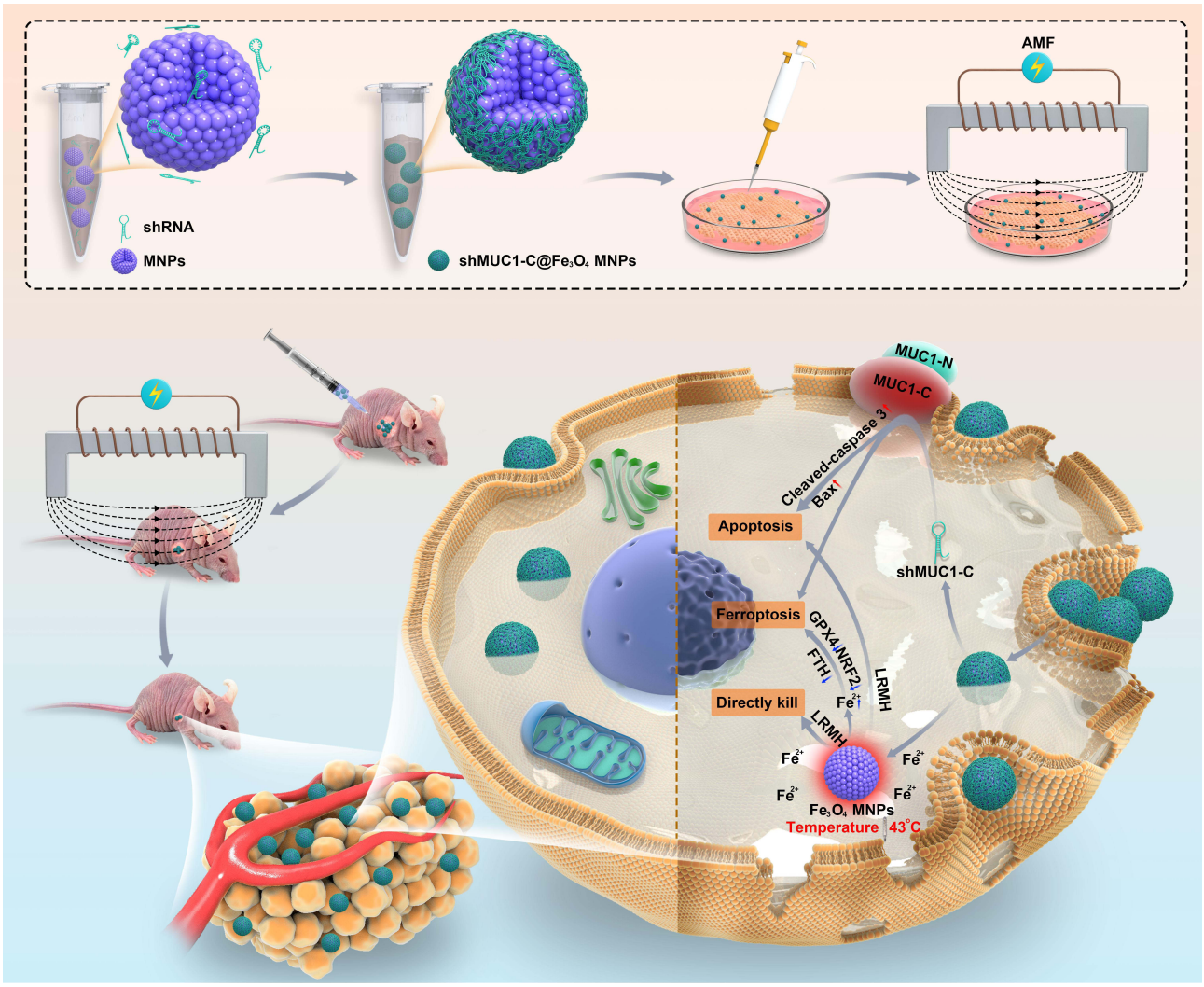

Scheme 2 Schematic illustration of MUC1-C shRNA@Fe_3O_4 MNPs construction and the therapeutic mechanism on TNBC. MUC1-C shRNA and Fe_3O_4 MNPs were self-assembled into MUC1-C shRNA@ Fe_3O_4 MNPs by electrostatic adsorption. After entering TNBC cells and under the action of AMF, on the one hand, it induces apoptosis and ferroptosis by targeting MUC1-C, on the other hand, it increases the temperature (43 °C) and the Fe^{2+} concentration directly kills TNBC cells and stimulates apoptosis and ferroptosis mechanisms.

Materials and Methods

Main Reagents

Fe_3O_4 MNPs and Fe_3O_4-FITC MNPs were obtained from Xi'an Rui Xi Biotechnology Co. (Xian, China); Trizol reagent was obtained from Invitrogen Life Technologies (CA, USA). MUC1-C shRNA plasmids were synthesized by Suzhou Jin Weizhi Co. Ltd, Jiangsu. The Transwell chamber (8.0 μm) was bought from Corning Inc. (NY, USA). Cell Counting Kit-8 (CCK-8) was purchased from Dojindo (Shanghai) Laboratories (Shanghai, China). 4',6-diamidino-2-phenylindole (DAPI), Ikarugamycin, Nystatin, Cytochalasin D, AntiGPX4, anti-NRF2, anti-FTH1, anti-Bax, and anti-Cleaved Caspase3 antibodies were from Abcam (Shanghai, China), Hematoxylin, Eosin staining kit, and Prussian blue stain Kit were acquired from Beyotime Biotechnology Co., Ltd. (Shanghai, China). All other reagents were purchased from Sigma Aldrich (Burlington, MA, USA).

Grouping

For the in vitro analysis, the TNBC cells were divided into (1) Control group: cells treated without any treatment; (2) Fe_3O_4 MNPs: cells treated with Fe_3O_4 MNPs but without AMF; (3) Fe_3O_4-shRNA MNPs: cells treated with MUC1-C shRNA@Fe_3O_4

MNPs but without AMF; (4) Fe_3O_4 MNPs+AMF: cells treated with Fe_3O_4 MNPs in AMF; (5) Fe_3O_4-shRNA MNPs +AMF: cells treated with MUC1-C shRNA@Fe_3O_4 MNPs and AMF. Groups 4 and 5 were treated with AMF at room temperature (26 °C) for 30 minutes, and the rest of the groups were placed at the same room temperature for the same time.

Similar to the grouping method mentioned above, in vivo analysis, TNBC xenograft tumor mice at the same stage with the same tumor burden were randomly divided into 5 groups (Control, Fe_3O_4 MNPs, Fe_3O_4-shRNA MNPs, Fe_3O_4 MNPs+ AMF, and Fe_3O_4-shRNA MNPs +AMF) and received different treatment measures.

Clinical Histopathological Analysis

The research was approved by the Ethics Committee of the Affiliated Hospital of Nanjing University of Chinese Medicine (ethical approval number: 2021NL-153-01). All experiments followed the *Declaration of Helsinki*. All included subjects were provided with their informed consent. Thirty BC tissues and para-cancerous tissues (>1.0 cm from the tumor margin) were obtained from postoperative specimens of TNBC patients (without preoperative radiotherapy and chemotherapy), and 16 normal breast tissues were obtained from postoperative specimens of benign breast tumors (>1.0 cm from the tumor margin) during the same period. All specimen wax blocks were obtained from patients who underwent surgical treatment for breast tumors between January 2021 and December 2021 at the Affiliated Hospital of Nanjing University of Chinese Medicine. The expression of MUC1 was determined by immunohistochemistry (IHC), and statistical analysis was performed.

Cell Lines and Culture

TNBC cell lines (BT-20, HCC-70, MDA-MB-468, and MDA-MB-231) and human normal mammary epithelial cell line (MCF-10A) were purchased from the Chinese Academy of Sciences Cell Bank (Shanghai, China). BT-20 and HCC-70 cell lines were cultivated in RPMI-1640 medium (Gibco). MDA-MB-468 and MDA-MB-231 cell lines were cultivated in Leibovitz's L-15 medium (Gibco). MCF-10A cell lines were cultured in MEGM (Lonza). All mediums contained 10% fetal bovine serum, 100 units mL^{-1} penicillin, and 100 μg mL^{-1} streptomycin. The incubation conditions were 37°C and 5% CO_2.

Animals

All animal experiments were approved by the Nantong University Animal Care and Use Committee (S20230522-004) and all of the animals were treated according to Nantong University's institutional guidelines established for animal care and use. 4–5 weeks-old female C-NKG (C001316) mice, weighing 18–20g, were purchased from Cyagen Research Center for Model Organisms (Jiangsu, China) and maintained in the SPF environment.

Construction and Verification of MUC1-C shRNA

MUC1 shRNAs (#1 TRCN0000122937, #2 TRCN0000430218, and #3 TRCN0000122938; MISSION shRNA; Sigma) which target the MUC1-C sequence GACACAGTTCAATCAGTATAA, and control scrambled shRNA (Sigma, not to target any known vertebrate gene) were inserted into the pLKO.1-puro vector. Cells were transfected with the MUC1-C shRNA plasmids, and then, the expression of MUC1-C shRNA mRNA and protein was tested by real-time PCR (RT-PCR) and Western blot methods. According to the results of gene silencing, the most effective plasmid would be selected to establish MUC1-C shRNA@Fe_3O_4 MNPs.

Preparation of MUC1-C shRNA @Fe_3O_4 MNPs

The Fe_3O_4 MNPs and MUC1-C shRNA plasmid solutions were ultrasonically dispersed firstly, then mixed at a certain volume ratio, and incubated in a water bath at 37°C with stirring (2000 rpm) for 4 h to promote binding; then the unencapsulated Fe_3O_4 MNPs and unbound MUC1-C shRNA plasmid were removed by high-speed centrifugation (12,000 rpm) and ultrafiltration membrane method; finally, powdered MUC1-C shRNA@ Fe_3O_4 MNPs was obtained by lyophilizer. Briefly, we prepared and purified MUC1-C shRNA@Fe_3O_4 MNPs using MUC1-C shRNA plasmid and Fe_3O_4 MNPs as raw materials by high-speed stirring, ultrafiltration, and freeze-drying methods in sequence.

Characterization of MUC1-C shRNA@Fe_3O_4 MNPs

Transmission electron microscopy (TEM) was implemented to observe the morphologic size of Fe_3O_4 and MUC1-C shRNA@Fe_3O_4 MNPs. TEM elemental mapping analysis was employed to verify the combination of MUC1-C shRNA plasmids and Fe_3O_4 MNPs. Dynamic light scattering (DLS) was implemented for the characterization of hydrodynamic dimensions and zeta potential of Fe_3O_4 and MUC1-C shRNA@Fe_3O_4 MNPs. Raman spectroscopy was used for the observation of MUC1-C shRNA molecular adsorption behavior of Fe_3O_4 MNPs. The encapsulation efficiency (EE) of MUC1-C shRNA in nanoparticles was measured and calculated by a NanoDrop-1000 spectrophotometer. O-phenanthroline spectrophotometry was used to determine the iron content of each sample, and a consistent iron content was set as the internal rule for different treatment measures. It was also used to compare the release of divalent iron ions under different pH and temperature conditions.

Cellular Uptake and the Uptake Pathways of MUC1-C shRNA@ Fe_3O_4 MNPs

HCC-70 cells were plated into 24-well plates for 24 h followed by incubation with FITC-labeled MUC1-C shRNA@ Fe_3O_4 MNPs (at a concentration of 200 ng mL^{-1}) for 3 h. Then the medium was removed, and cells were washed with PBS thrice to eliminate unbound residue.

Afterward, 4.0% paraformaldehyde (PFA) was added to fix cells, 2μg mL^{-1} DAPI was used to stain cell nuclei, and confocal laser scanning microscopy (CLSM) was employed to observe the results. For the cellular uptake pathway investigation, HCC-70 cells were preincubated with one of the following endocytosis inhibitors dissolved in serum-free DMEM: Nystatin (a caveolae-mediated cell uptake inhibitor), Ikarugamycin (IKA, clathrin-associated endocytosis inhibitor) and Cytochalasin D (CD, a macropinocytosis-dependent endocytosis inhibitor) for 30 min, and then the steps described in cellular uptake experiments were repeated. Intracellular fluorescence was observed under CLSM.

Magneto-Thermal Conversion of MUC1-C shRNA@Fe_3O_4 in AMF

For the Magneto-Thermal thermal conversion research, the MUC1-C shRNA@Fe_3O_4 MNPs (v:1.0 mL) with concentrations of 50 μg mL^{-1}, 100 μgmL^{-1}, 150 μg mL^{-1}, 200 μg mL^{-1}, and 250 μg mL^{-1} were put into flat-bottomed test tubes (10 mm diameter), respectively, and put into an alternating magnetic inductor (AMI) (ZDBT-6, Shanghai Hanggong, China) after a water bath at 26 °C for 5 minutes. The distance from the bottom of the test tube to the center of the AMI coil was 10 mm, the output power of the AMI was set to 3 kW for 60 minutes, and the temperature was recorded every 5 minutes to record the data. The heating curves were plotted at different concentrations with temperature as the vertical coordinate and time as the horizontal coordinate. Solution temperature data were obtained by an electronic thermometer (TESTO-720-Pt100, TESTO, China).

Hemolysis Test

The hemolysis assay was used to assess the biocompatibility of MUC1-C shRNA@Fe_3O_4 MNPs with red blood cells (RBCs). Fresh blood was obtained from New Zealand rabbits donated by Nantong University Laboratory Animal Center. RBCs were collected by centrifugation of the blood at 1500 rpm for 15 min, followed by three washes with PBS (pH 7.4). The RBCs (4% w/v) were then incubated with different concentrations of MNPs at a ratio of 1:9 v/v for 3 h at 37°C, respectively, followed by centrifugation at 3000 rpm for 15 min. Distilled water was set as a positive control and PBS was set as a negative control. The extract supernatants were measured by ultraviolet-visible (UV-vis) spectroscopy at 545 nm for OD values (Shimadzu UV-Vis Spectrophotometer UV-1700; Shimadzu, Kyoto, Japan). Hemolysis was calculated according to the following equation:

$$Hemolysis\ rate(\%) = \frac{[OD(sample) - OD(negative\ control)]}{[OD(positive\ control) - OD(negative\ control)]} \times 100\%$$

RT-qPCR

RNAiso Plus (Takara, Japan) kit was adopted for total RNA isolation according to the instructions provided by the manufacturer. Then RNA was reversely transcribed using M-MLV reverse transcriptase (Promega, WI, USA), followed by PCR quantification

via SYBR qPCR mix kit (Toyobo Life Science, Japan). GAPDH was applied as the internal control. The sequences of the primers were as follows: MUC1 Forward, 5'-TCTGCCCAGAATCCGACAAC-3' and Reverse, 5'-AATGTCTTTACGAGC AGTGGTAG-3'; GAPDH Forward, 5'- TGTGGGCATCAATGGATTTGG-3' and Reverse, 5'- ACACCATGTATTCC GGGTCAAT-3'. The $2^{-\Delta\Delta Ct}$ method was used for quantifying gene expression.

Western Blot

The protein concentration was measured by BCA methods. Then proteins were undergone 10% sodium dodecyl sulfate–polyacrylamide gel electrophoresis (SDS-PAGE) and transferred to a polyvinylidene difluoride membrane. Next, skimmed milk (5%) was adopted for blocking the membrane, followed by cultivation with the primary antibodies, including MUC1 (ab109185, 1:2000, Abcam), GPX4 (ab125066, 1:2000, Abcam), NRF2 (ab62352, 1:2000, Abcam), FTH1 (ab183781, 1:2000, Abcam) and GAPDH (ab9485, 1:5000, Abcam). After washing, the membrane was incubated with the secondary antibodies. The protein bands were assessed via the ECL system and imaged by the Tanon 4600 imaging system.

Wound Healing Assay

Cells (1×10^5 cells/well) were planted into 24-well plates. Wounds were created by a plastic tip. The width of the scratch was observed by an inverted microscope and photographed at 0 h and 24 h.

Transwell Assay

In brief, cells were planted with Matrigel (BD Biosciences) into the upper chamber of the Transwells. Medium containing 10% FBS was put into the lower chamber. 24 h later, the upper chamber was removed and fixed with 4% paraformaldehyde. The lower chamber containing the invaded cells was collected and then fixed and stained. The cells were observed using an inverted microscope.

Cell Counting Kit-8 (CCK-8) Assay

The viability of breast cancer cells was assayed by the CCK-8 kit. Briefly, after receiving different treatment measures, each group of cells was inoculated into 96-well plates at a density of 5×10^3 cells/well and incubated at 37°C in the 5% CO_2 incubator, after 12 h (and 24, 48.72 h), 10 μL of CCK-8 reagent was added to each well and incubated for 4 h. The absorbance at 450 nm was measured using a microplate reader (Thermo Fisher, United States). The cell proliferation inhibition rate was calculated using this formula:

$$IR = \left[1 - \frac{OD(experimental\ group) - OD(blank)}{OD(control\ group) - OD(blank)}\right] \times 100\%$$

In vivo Combined Therapies and Biosafety

For the in vivo analysis, TNBC cells (5×10^6) were injected into the right axillary dorsal subcutaneous area of 6-week-old female C-NKG (C001316) mice to establish TNBC xenograft tumor models. When the tumor volumes reached 100 mm^3, those mice were randomly divided into five groups according to the grouping plan described above (4 mice for each group). Saline or Fe_3O_4 MNPs (200 μg mL^{-1}) or MUC1-C shRNA@Fe_3O_4 MNPs (200 μg mL^{-1}) were injected into the tumor (at multiple points: above, below, left, right, and behind the tumor). Under the premise of the above concentration, the ratio of injected dose to tumor volume is 1:1. After injection, all mice were placed in the AMF for 30 minutes. The magneto-thermal performances of MUC1-C shRNA@Fe_3O_4 MNPs in vivo were recorded by IR thermal camera (HIKMICRO-H10, Hikvision, China). Repeat injection and treatment every 5 days, measure the size of the tumor and body weights before injection. Tumor volume was calculated as $V = 0.52\times L\times W^2$, where L and W are the larger and smaller diameters, respectively. After 25 days, the mice in each group were sacrificed and the tumors were collected, imaged, measured, and weighed. The relative tumor volume (RTV) and relative tumor proliferation rate T/C (%) were calculated based on the tumor volume measured at different time points with the following equations

$$RTV = \frac{V_t}{V_0}$$

$$T/C(\%) = \frac{RTV(treatment\ group)}{RTV(control\ group)} \times 100\%$$

Based on the weight of the tumor specimen, the tumor growth inhibition value (TGI, TGI < 40% was considered ineffective; TGI ≥ 40% and statistically treated with P< 0.05 was considered effective.) and the combination index (Q_{50} method, Effect A (EA): TGI of MUC1-C shRNA@Fe_3O_4 MNPs, Effect B (EB): TGI of Fe_3O_4 MNPs+AMF, and Effect AB[E (A+B)]: TGI of MUC1-C shRNA@Fe_3O_4 MNPs+AMF; When q ≥1.15, it indicates synergistic effect between the two treatments) were calculated by the following equations:

$$TGI(\%) = \left[1 - \frac{Treatment\ group(tumor\ weight)}{Control\ group(tumor\ weight)}\right] \times 100\%$$

$$q = \frac{E(A+B)}{EA + EB - EA \times EB}$$

The tumor, liver, spleen, kidneys, lungs, and heart were harvested, sliced, and stained with hematoxylin-eosin. Tumour tissue specimens were restained with Prussian blue to observe the infiltration of Fe^{2+} in the tissue. The serum samples were separated from the collected blood (N = 4), and the biochemical indices, including aminotransferase (AST), alanine aminotransferase (ALT), total bilirubin (TBIL), alkaline phosphatase (ALP), blood urea nitrogen (BUN), and creatinine (CR) were assessed using commercially available kits according to the manufacturer's protocols.

Statistical Analysis

All data were assessed using GraphPad Prism 9.5.1 and were indicated as mean ± standard deviation. Statistical significance (p-values) was calculated by Fisher's exact test (two-sided), One-way or Two-way ANOVA followed by Tukey honestly significantly different (HSD) post hoc test. Asterisks represent: *p<0.05, **p<0.01, ***p<0.005, ****p<0.001.

Results

MUC1 Overexpressed in TNBC

Based on the results of the Human Protein Atlas (HPA), UCSC Genome Browser on Human (GRCh38/hg38), and the Cancer Genome Atlas (TCGA) datasets, MUC1 was highly expressed in BC (Figure 1A, B and D) and BC cell lines (Figure 1C). Similarly, our RT-PCR analysis confirmed that MUC1 expression was significantly elevated in TNBC cell lines (BT-20, HCC-70, MDA-MB-468, and MDA-MB-231) compared to human normal mammary epithelial cell line MCF-10A, (p<0.01) (Figure 1E). The tendency was consistent with the results from the HPA database (Figure 1C). In the IHC analysis, the expression rate of MUC1 in TNBC was 53.33% (16/30) significantly higher than that in normal breast tissues 18.75% (3/16) and para-cancerous tissue 23.33% (7/30), p<0.05 (Figure 1F). Subsequently, we selected MUC1 high-expressed HCC-70 and MDA-MB-468 cell lines for the in vitro research and employed HCC-70 cells to construct the xenograft tumor model for in vivo research.

Construction and Verification of MUC1-C shRNAs

According to the RT-qPCR (Figure 2A) and WB results (Figure 2B and C), we observed that MUC1 expression was reduced after transfection of MUC1-C shRNA 1#, MUC1-C shRNA 2# and MUC1-C shRNA 3#. Moreover, the inhibitory effect of shRNA 3# was better than others, so we selected MUC1-C shRNA 3# for further experiments. Figure 2D and E show the plasmid map and sequence of selected MUC1-C shRNA 3#.

Characterization of MUC1-C shRNA@Fe_3O_4 MNPs

The MUC1-C shRNA@Fe_3O_4 MNPs suspension we prepared has a black-brown appearance (Figure 3A).

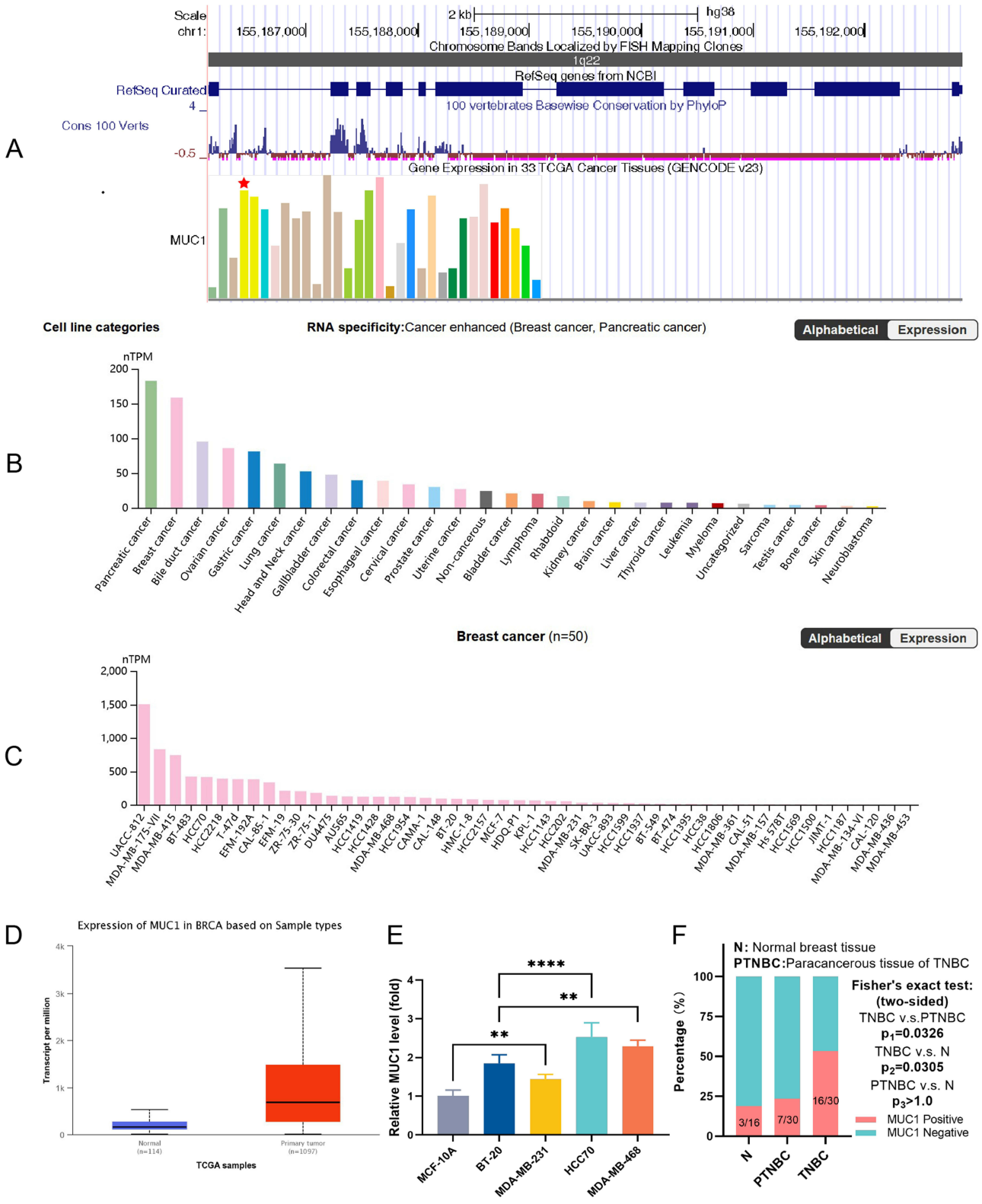

Figure 1 MUC1 and its expressions in various types of tumors (from UCSC genome browser on human, the red pentagram indicates breast invasive carcinoma) (**A**), MUC1 protein expression in different tumor cell lines (**B**) and BRCA cell lines (**C**) (based on datasets of Human Protein Atlas), MUC1 expression between BRCA and normal tissue (**D**) (based on datasets of The Cancer Genome Atlas), MUC1 expression in normal human breast cell (MCF-10A) and TNBC cell lines (BT-20, MDA-MB-231, MDA-MB-468, HCC-70) (**E**). IHC results of MUC1 in TNBC tissues, paraneoplastic tissues and normal breast tissues (**F**). Error bars represent means ± SD. **p<0.01, ****p<0.001.

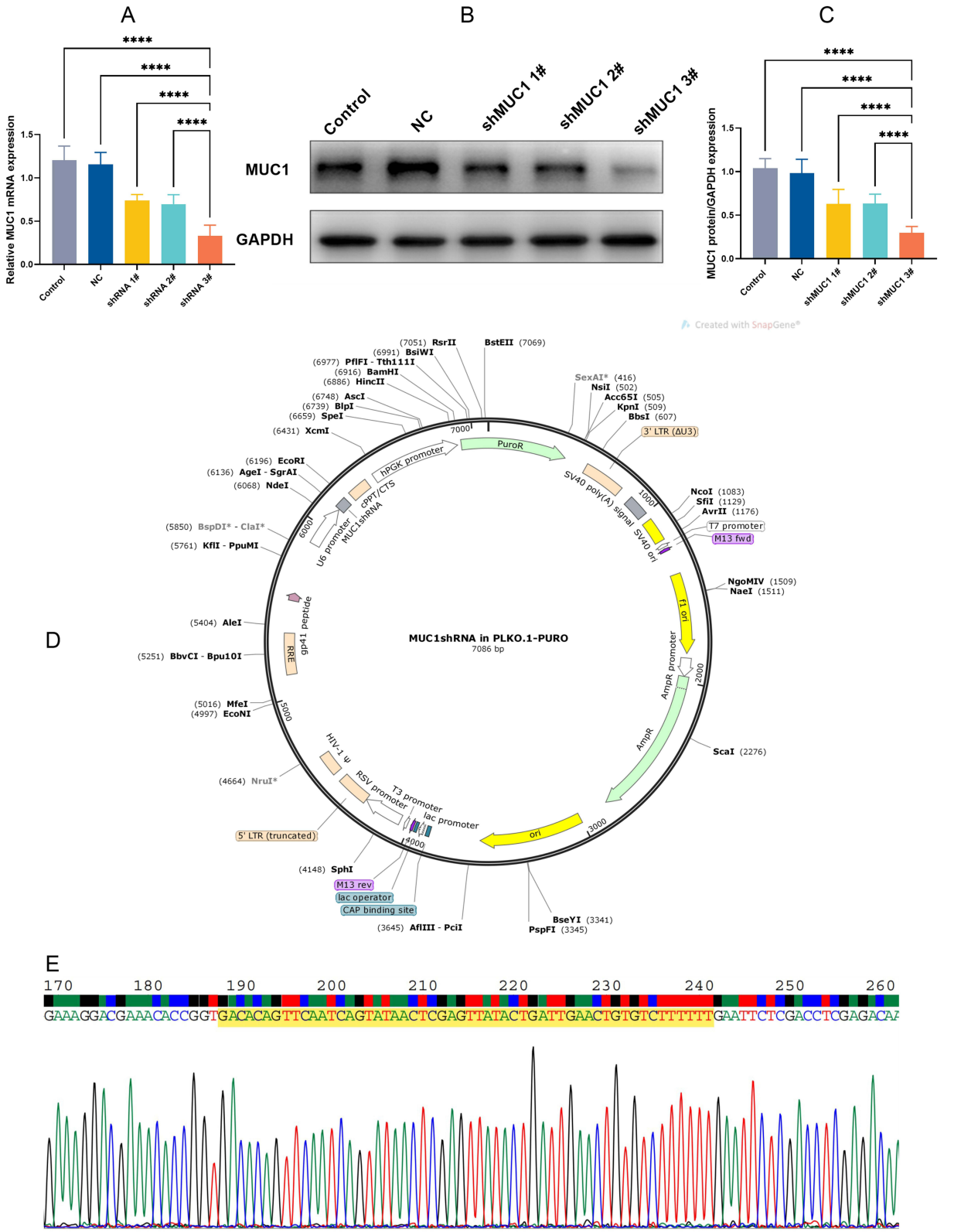

Figure 2 Silence efficiency of MUC1-C shRNA on TNBC cell line HCC-70. RT-qPCR (**A**) and Western blot detected the silencing efficiency of MUC1-C shRNA (**B** and **C**). MUC1-C shRNA (3#) plasmid map (**D**) and target sequence (the highlighted yellow section) (**E**). Error bars represent means ± SD. ****p<0.001.

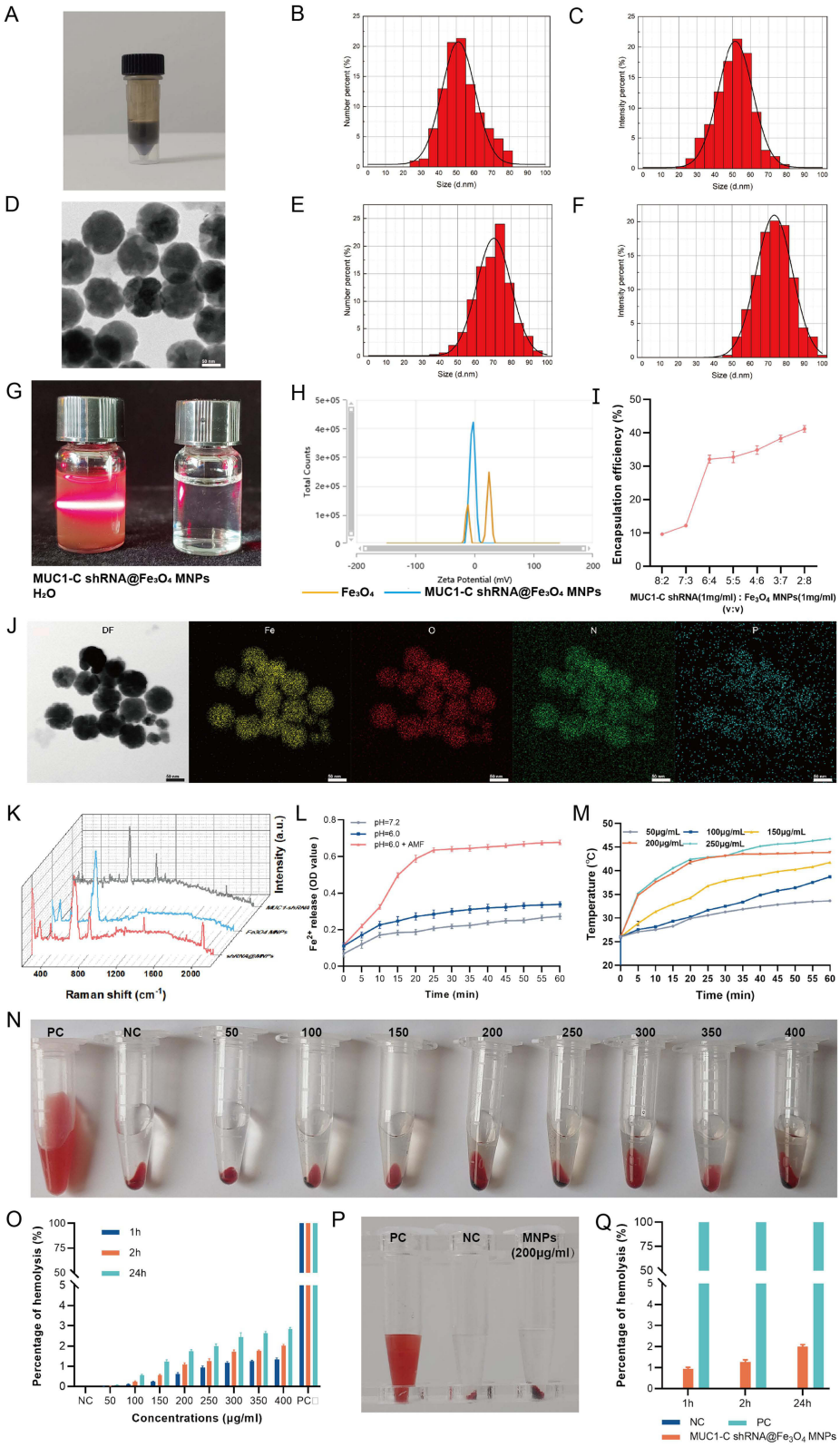

Figure 3 Characterization of MUC1-C shRNA@Fe_3O_4 MNPs. Appearance (**A**) and TEM image (**D**) of the prepared MUC1-C shRNA@Fe_3O_4 MNPs. DSL Size distribution of Fe_3O_4 MNPs (**B** and **C**) and MUC1-C shRNA@Fe_3O_4 MNPs (**E** and **F**). Tyndall effect of MUC1-C shRNA@Fe_3O_4 MNPs (**G**). Zeta potential of MUC1-C shRNA@Fe_3O_4 MNPs (**H**). Encapsulation efficiency at different shRNA/MNPs ratios (**I**). TEM elemental mapping analysis of MUC1-C shRNA@Fe_3O_4 MNPs (**J**). Raman spectrum of MUC1-C shRNA, Fe_3O_4 MNPs, and MUC1-C shRNA@Fe_3O_4 MNPs (**K**). Release profiles of Fe^{2+} from MUC1-C shRNA@Fe_3O_4 MNPs at different pH values with or without AMF (**L**). The heating curves of MUC1-C shRNA@Fe_3O_4 MNPs with different concentrations (50–250μg/mL) (**M**). Hemolysis test at different concentrations (MUC1-C shRNA@Fe_3O_4 MNPs) (n=3) (**N** and **O**). Hemolysis test (200μg/mL, n=3) (**P** and **Q**). Error bars represent means ± SD. TEM scale bar: 50nm.

Through the TEM and DLS detection, the average size of Fe_3O_4 MNPs increased from 50 to 75 nm (Figure 3B–F) after binding negatively charged MUC1-C shRNA on the surface. The prepared MUC1-C shRNA@Fe_3O_4 MNPs solution showed the Tyndall effect under laser irradiation, while the control group (water) did not (Figure 3G). TEM elemental mapping analysis was used to analyze the chemical composition of MUC1-C shRNA@Fe_3O_4 MNPs. From the results (Figure 3J), we found that in addition to Fe and O elements, there were also N and P elements contained in the MUC1-C shRNA@Fe_3O_4 MNPs, indicating that Fe_3O_4 MNPs adsorbed MUC1-C shRNA. From Raman spectrum analysis (Figure 3K), we observed that the prepared nanoparticles showed both the characteristic peak of Fe_3O_4 ($665cm^{-1}$) and the characteristic peak of the skeleton phosphate group of shRNA ($815cm^{-1}$). On the other hand, the changes in zeta potential also confirmed the adsorption binding of MUC1-C shRNA to Fe_3O_4 MNPs. Since the magnetic transfection reagent diluted with PBS may affect the shift of Zeta potential, which generally reached a value near 0 in PBS, and presented two peaks, which tended to be negative after MUC1-C shRNA binding, indicating that MUC1-C shRNA indeed bound with Fe_3O_4 (Figure 3H). Entrapment rates of MUC1-C shRNA@Fe_3O_4 MNPs prepared with different volume ratios of MUC1-C shRNA and Fe_3O_4 MNPs are shown in Figure 3I. It was observed the EE significantly increases at the 6:4 volume ratio. With the increase in the proportion of Fe_3O_4 MNPs, the EE did not rise significantly, indicating that the MUC1-C shRNA EE was optimized at a concentration of 6:4, EE: (29.78 ± 0.63) %. Subsequently, the trend of Fe^{2+} release from MUC1-C shRNA@Fe_3O_4 MNPs in vitro was explored through phenanthroline spectrophotometry (Figure 3L). Under thermal stimulation (43°C), the release of Fe^{2+} was significantly higher in the acidic environment (pH=6.0) surrounding the simulated tumor than in the physiological and acidic environment without thermal stimulation.

We also explored the magneto-thermal conversion ability of different concentrations of MUC1-C shRNA@Fe_3O_4 MNPs under a given AMF (3Kw). As shown in Figure 3M, the MUC1-C shRNA@ Fe_3O_4 MNPs magnetic fluid (200 μg mL^{-1}) rapidly warmed within 20 minutes and stably maintained at about 43 °C within 30 minutes. Based on the magneto-thermal conversion curves, the optimal MUC1-C shRNA@ Fe_3O_4 MNPs concentration (200 μg mL^{-1}) was selected for the following experiments.

The hemolysis test responds to the biocompatibility of nanoparticles, within the concentration range (50–400 μg mL^{-1}) and time range (1 h, 2 h, 24 h) that we observed, the hemolysis rates of MUC1-C shRNA@Fe_3O_4 MNPs were less than 3% (Figure 3N and O). Specifically, at the concentration (200 μg mL^{-1}) used for the cellular and animal experiments, the hemolysis rates were (0.945±0.069)% at 1 h, (1.258±0.111)% at 2 h, and (1.995±0.102)% at 24 h, respectively (Figure 3P and Q and Table S1).

Cellular Uptake and Internalization Mechanism of MUC1-C shRNA@ Fe3O4 MNPs in HCC-70 Cells

The qualitative cellular uptake of MUC1-C shRNA@ Fe_3O_4 MNPs in HCC-70 cells was measured by CLSM. Average fluorescence intensity semi-quantitative analysis was measured through ImageJ software. The uptake of MUC1-C shRNA@ Fe_3O_4 MNPs in the cells was visualized by the fluorescence intensity of FITC (green) while the cell nuclei were shown by DAPI (blue). As shown in Figure 4A, the green fluorescence was observed in the cytoplasm of the HCC-70 cells after 3 h of incubation. The average fluorescence intensity of the other three cells pretreated with cytosolic inhibitor Nystatin, IKA, and CD decreased by 44.3%, 49.7%, and 14.1% respectively (Figure 4B). These results suggested that the clathrin-associated endocytosis pathway and caveolae-mediated cell uptake pathway played vital roles in the internalization of MUC1-C shRNA@ Fe_3O_4 MNPs.

Therapeutic Effects and Biosafety of MUC1-C shRNA@Fe_3O_4 MNPs in vitro

The wound healing assays and Transwell assays reflected the effects of MUC1-C shRNA@Fe_3O_4 MNPs combined with AMF on the migration and invasion of TNBC cells. In the wound healing assays, the migration ability of HCC70 cells in Fe_3O_4-shRNA+AMF group was significantly lower than other groups: Fe_3O_4-shRNA+AMF group (20.50%) VS Control group (78.86%), Fe_3O_4 group (75.28%), Fe_3O_4-shRNA group (61.73%), and Fe_3O_4+AMF group (35.49%), $p<0.05$ (Figure 5A). Similar results were observed in the Transwell assays (Figure 5B). Moreover, the trends of CCK-8 OD values of different groups at different time points are shown in Figure 5C. According to CCK-8 results, the inhibition rate

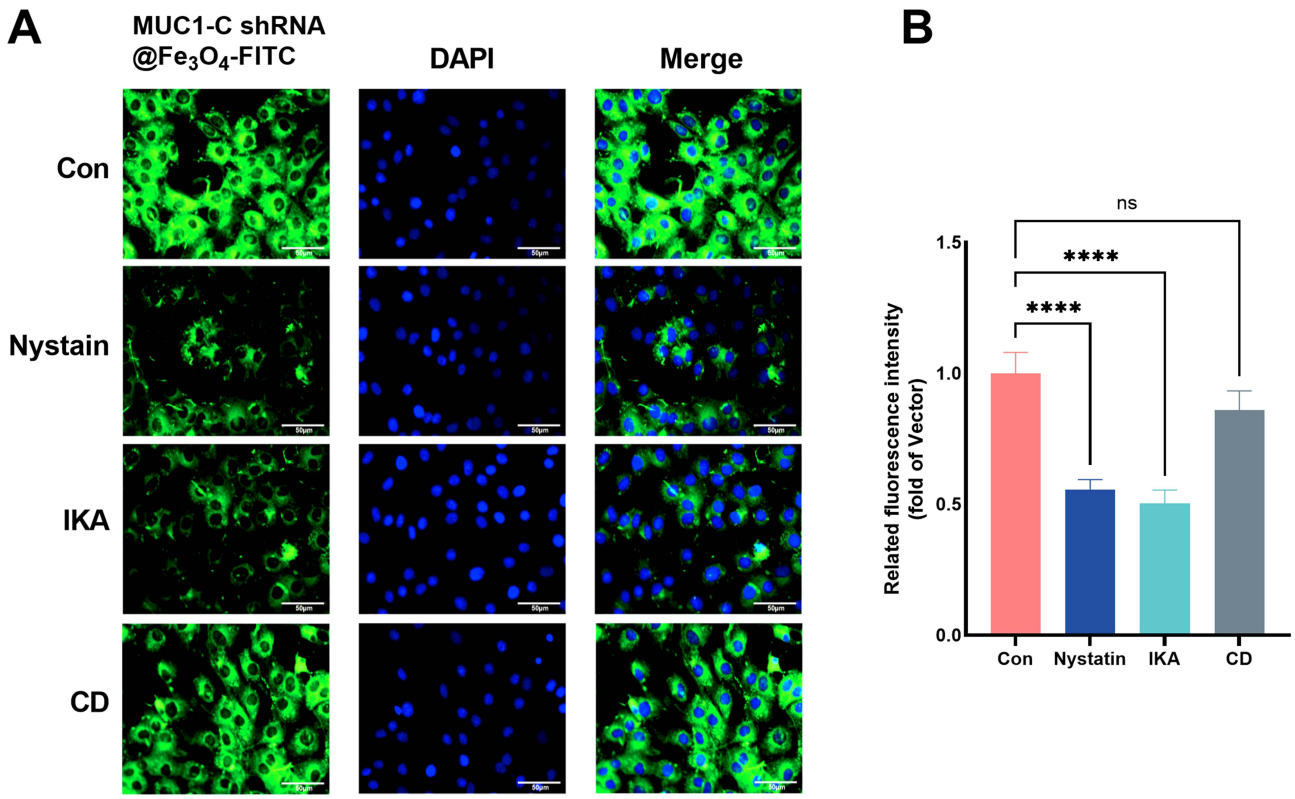

Figure 4 Cellular uptake of NPs. Cellular uptake of MUC1-C shRNA@Fe_3O_4 MNPs in the HCC-70 cells was observed under a CLSM. Green fluorescence indicates MUC1-C shRNA@Fe_3O_4-FITC and blue fluorescence indicates the nucleus (**A**). Investigation of internalization pathway of MUC1-C shRNA@Fe_3O_4 MNPs in HCC-70 cells in the presence of different endocytosis inhibitors (n=3) (**B**). Error bars represent means ± SD. Scale bar: 50μm. ****p<0.001.

of HCC-70 cells in Fe_3O_4 group at 12, 24, 48, and 72 h were (1.72 ± 0.77) %, (5.36 ± 1.14) %, (10.38 ± 0.95) %, and (12.96 ± 1.94) %. Correspondingly, the results of Fe_3O_4-shRNA group, Fe_3O_4+AMF group, and Fe_3O_4-shRNA+AMF group were [(5.79 ± 2.83) %, (12.32 ± 1.22) %, (21.58 ± 1.85) %, and (23.32 ± 1.89) %], [(39.20 ± 3.01) %, (41.44 ± 2.72) %, (45.17 ± 3.48) %, and (52.59 ± 1.88) %], and [(45.26 ± 1.24) %, (58.45 ± 2.08) %, (77.92 ± 2.61) %, and (91.12 ± 2.36) %] (Figure 5D and E).

Finally, we detected the protein expression levels of ferroptosis-related proteins (GPX4, NRF2, and FTH1) and apoptosis-related factors (Bax and cleaved-caspase3) by Western blot (Figure 5F) and performed statistical analysis on them (Figure 5G). As shown in Figure 5G, compared with the control, the expressions of ferroptosis-related proteins GPX4, NRF2, and FTH1, specifically GPX4 and NRF2 significantly decreased in the Fe_3O_4-shRNA+AMF group. The expressions of apoptosis-related protein Bax and cleaved-caspase3 was elevated in the Fe_3O_4-shRNA, and Fe_3O_4+AMF groups, especially the Fe_3O_4-shRNA+AMF group.

We also repeated the same experiments in MDA-MB-468 cell lines and obtained similar results (Supplementary Figure 1).

Therapeutic Effects and Biosafety of MUC1-C shRNA@Fe_3O_4 MNPs in vivo

Encouraged by the good antitumor effect in vitro, we further investigated the tumor suppressive effect of MUC1-C shRNA@Fe_3O_4 MNPs in AMF on TNBC xenograft models. The in vivo magneto-thermal properties of MUC1-C shRNA@Fe_3O_4 MNPs in AMF were confirmed by the infrared thermal imaging camera. As shown in Figure 6A, after multiple injections of MUC1-C shRNA@Fe_3O_4 MNPs into the tumor site, the temperature around the tumor reached 43 degrees Celsius after 20 minutes of exposure to AMF (3 Kw), continuing the AMF effect and the heating range further increasing. This temperature can be maintained stably for more than 30 minutes, while the control group has no magnetothermal reaction. The images of tumors in different groups were shown in Figure 6B. After 25 days of different treatments, the tumor weight (Figure 6C) and volume (Figure 6D) in the Fe_3O_4 group did not significantly change in

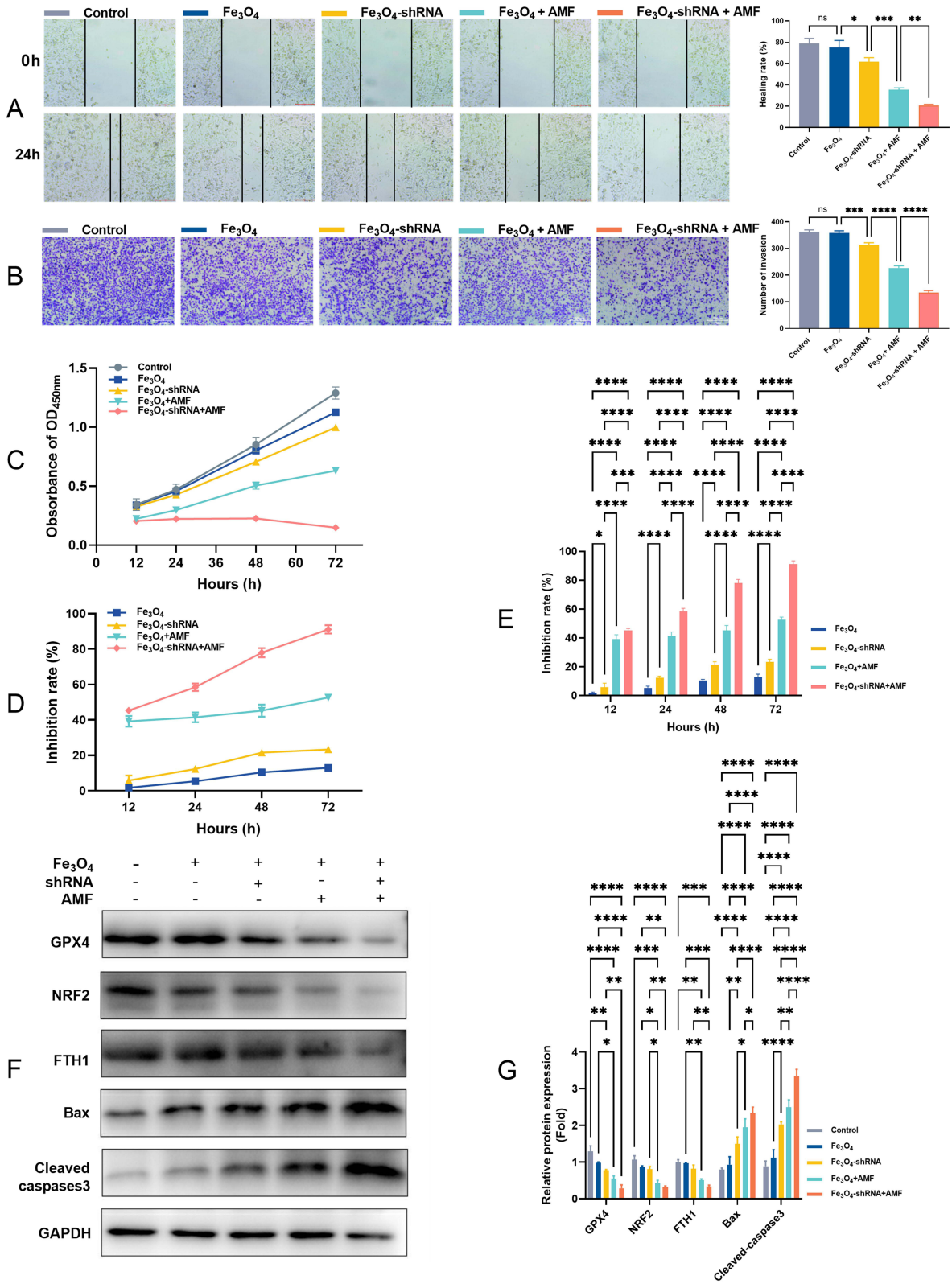

Figure 5 MUC1-C shRNA@Fe_3O_4 MNPs suppress the migration, invasion, and proliferation in HCC-70 cell lines. Wound healing (**A**), Transwell (**B**), CCK-8 OD_{450nm} (**C**), and inhibition rate based on CCK-8 (**D** and **E**). The protein bands (**F**) and quantitative statistical results (**G**) of Bax, cleaved-caspase3, GPX4, NRF2, and FTH1 of HCC-70 cell lines (n=3). Error bars represent means ± SD. *p<0.05, **p<0.01, ***p<0.005, ****p<0.001.

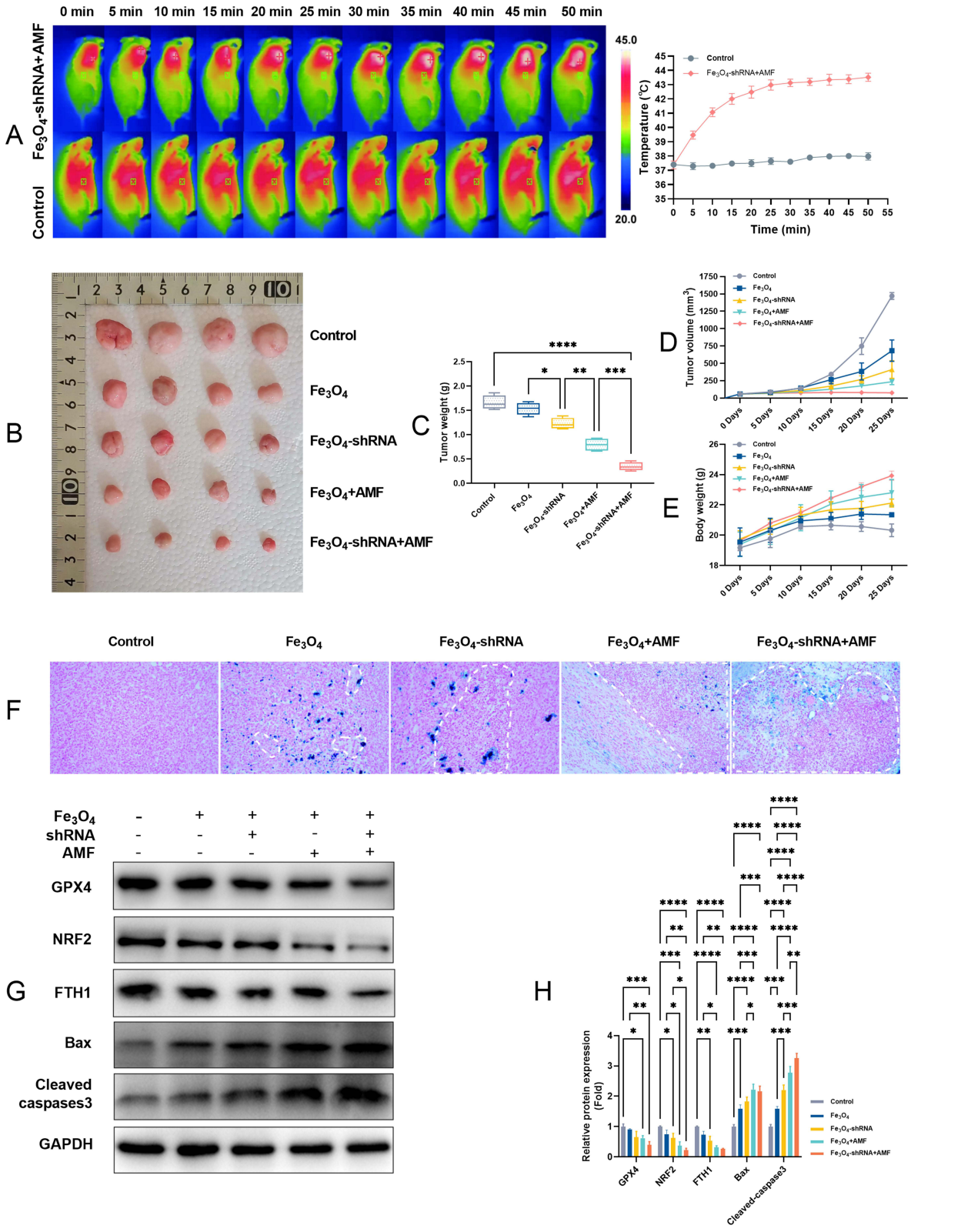

Figure 6 The in vivo therapeutic effects of the MUC1-C shRNA@Fe_3O_4 MNPs on TNBC. IR thermal images of TNBC-bearing C-NKG mice with local injection of MUC1-C shRNA@Fe_3O_4 MNPs (200 μg mL^{-1}), or normal saline under AMF (3Kw) (**A**). Images (**B**) and weights (**C**) of xenograft tumors harvested from the mice after various treatments on the 25th day. Tumor volumes (**D**) and Body weight (**E**) growth in mice were measured after different treatments every 5 days within 25 days (n=4). Prussian blue reaction of tumor tissue showing iron staining and tumor necrosis, labeled area was typical necrosis (200x) (**F**). Expression of Bax, cleaved-caspase 3, GPX4, NRF2, and FTH1 in tumor tissues (**G**). Quantitative statistical results according to the protein bands (**H**). Error bars represent means ± SD. *p<0.05, **p<0.01, ***p<0.005, ****p<0.001.

https://doi.org/10.2147/IJN.S426849 DovePress

contrast to the control group ($p<0.05$). Besides, in comparison with the control group, the tumor weight and volume of the Fe_3O_4-shRNA and Fe_3O_4 +AMF groups decreased, especially in the Fe_3O_4-shRNA+AMF group. The animals in the Fe_3O_4-shRNA+AMF group showed an advantage in body weight at day 15, which continued to increase after that, and overall the other four groups at day 25 (with statistical significance) (Figure 6E).

Based on the tumor weights, we calculated the tumor growth inhibition (TGI) rates for different treatment groups (Fe_3O_4, Fe_3O_4-shRNA, Fe_3O_4+AMF, and Fe_3O_4-shRNA+AMF group) were 7.37%, 26.01%, 52.19%, and 79.22%, respectively (Tables S2). As key treatment measures, shRNA gene therapy and magnetic hyperthermia showed synergistic therapeutic effects in Fe_3O_4-shRNA+AMF, with a combination index (*q index*) of 1.23 (>1.15) (Tables S2).

In addition, from the date of transplantation tumor volume at different time points, we calculated the relative tumor proliferation rate T/C (%) of different treatment groups at different time points, the values on 25th day were 47.56%, 27.82%, 16.77%, and 5.26%, respectively (Tables S3). Where the values of the Fe_3O_4-shRNA, Fe_3O_4 +AMF, and Fe_3O_4-shRNA+AMF groups were less than 40% and showed statistical differences. Prussian blue reaction examination of tumor tissues in different groups showed iron (shown in blue) and varying degrees of tissue necrosis (typical areas were marked with a dotted line), with tumor necrosis being most significant in the Fe_3O_4-shRNA+AMF group (Figure 6F).

Moreover, WB results (Figure 6G) showed the expressions of GPX4, NRF2, and FTH1 were suppressed while Bax and cleaved-caspase3 were significantly increased in the Fe_3O_4-shRNA+AMF group. The results of protein expression statistics (Figure 6H) in animal-level studies showed the same trend as the results of the aforementioned cellular-level studies.

Finally, we evaluated the potential toxicity of MUC1-C shRNA@Fe_3O_4 MNPs in vivo under AMF conditions by serum biochemistry analyses and pathological examinations. Serum biochemical parameters, including ALT, AST, ALP, TBIL, BUN, and CR presented negligible discrepancies in all mice (Figure 7A). Besides, hematoxylin-eosin staining images of the major organs including the heart, lung, spleen, kidney, and liver indicated no obvious abnormal pathological changes in each group (Figure 7B).

Discussion

In this study, we employed MUC1-C shRNA as the MUC1 gene target drug, and Fe_3O_4 MNPs as the carrier to construct a functional MUC1-C shRNA@ Fe_3O_4 MNPs, and explored the therapeutic effects of the gene therapy combined with hyperthermia treatment strategy on TNBC in vitro and in vivo. Our data suggested MUC1-C shRNA@Fe_3O_4 MNPs can exert magnetic hyperthermia and anti-tumor effects, the results of current work may provide a potential option for the management of TNBC.

Results of many previous studies suggested that for the treatment of cancers, nanoparticles have shown good biocompatibility, low toxicity as well as biodegradability, and were considered as suitable carriers for the delivery of anti-tumor genes, antibodies, or anti-tumor drugs. For example, Fan et al designed a new type of nanoparticles that carried CD276 bispecific antibodies as well as MMP-2 genes, and they found the nanoparticles could induce ferroptosis on glioblastoma cells both in vitro and in vivo;[34] moreover, Li et al prepared the cationic lipid-assisted nanoparticles containing CD47 siRNA as well as R848, to increase the therapeutic efficacy of anti-TNBC therapies;[35] in our team, we previously designed PEG-MZF-NPs nanoliposomes containing CD44-shRNA as well as cisplatin, and the nanoliposomes showed excellent anti-tumor effects and low toxicity on ovarian cancer cells.[36]

In the current study, we prepared MUC1-C shRNA@Fe_3O_4 MNPs, and the properties of the nanoparticles were characterized by TEM, Zeta potential, Raman, and DLS; meanwhile, the stable binding between MUC1-C shRNA and Fe_3O_4 MNPs were also confirmed. Taken together, these results suggested that the MUC1-C shRNA@Fe_3O_4 MNPs were successfully prepared. Moreover, results of the hemolysis test suggested the hemolysis rates of MUC1-C shRNA@Fe_3O_4 MNPs were (0.945±0.069)% at 1 h, (1.258±0.111)% at 2 h and (1.995±0.102)% at 24 h, which were by the international safety standards for biomaterials (<5%). By studying the magneto-thermal conversion of MUC1-C shRNA@Fe_3O_4 MNPs under different concentrations and magnetic field strength conditions in vitro, we found that under the conditions

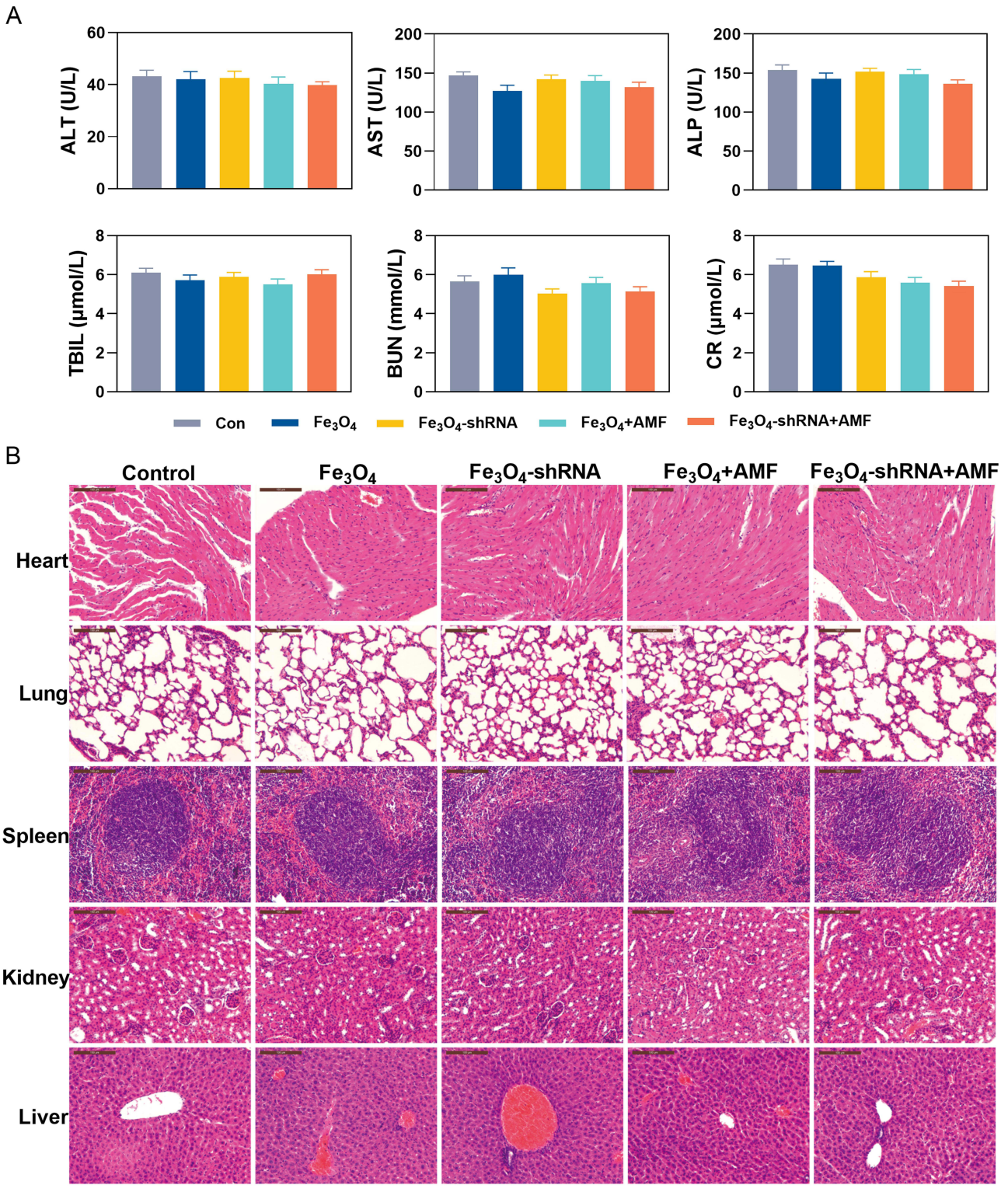

Figure 7 Serum biochemistry indicators assessment of TNBC mice (n=4). Alanine aminotransferase (ALT), Aspartate aminotransferase (AST), Alkaline phosphatase (ALP), Total bilirubin (TBIL). Blood urea nitrogen (BUN), Creatinine (CR) (**A**). Effect of MUC1-C shRNA@Fe_3O_4 MNPs on the histopathology of heart, lung, spleen, Kidney, and liver from TNBC mice (**B**). Error bars represent means ± SD. Scale bar: 100μm.

of nanoparticle concentration of 200 μg mL^{-1} and output of 3Kw, MUC1-C shRNA@Fe_3O_4 MNPs were able to increase the temperature to a therapeutic temperature of about 43 °C within 20 minutes and maintain it stably after 30 minutes, which fits well with the temperature conditions required for moderate hyperthermia of tumors.

The anti-tumor effects of MNPs under magnetic fields have been reported in previous studies. For example, Hernandes et al designed doxorubicin-loaded magnetic nanoparticles, and they found the nanoparticles could inhibit the growth as well as migration of MCF-7 cells;[37] Meenakshi et al designed polypropylene sulfide-coated MNPs with good biocompatible and therapeutic efficacy for cancer treatment.[38] In the current work, we analyzed the therapeutic effects of the MUC1-C shRNA@Fe_3O_4 MNPs on TNBC under the effect of AMF. In vitro experiments showed that our MUC1-C shRNA@Fe_3O_4 MNPs could effectively inhibit the proliferation, migration, and invasion of TNBC cells. The in vivo experiments also confirmed that the MUC1-C shRNA@Fe_3O_4 MNPs could produce good therapeutic effects in the AMF, and the tumor size of the MUC1-C shRNA@Fe_3O_4 MNPs+AMF group was significantly reduced in comparison with that of the other groups, and the weight change of the animals during the treatment, the serum biochemical indexes and the pathological section of important internal organs after the treatment confirmed that our MUC1-C shRNA@Fe_3O_4 MNPs had no obvious toxic side effects. Furthermore, WB results showed that Bax and cleaved-caspase3 protein (which are considered to be apoptosis-promoting biomarkers) expressions were significantly up-regulated after MUC1-C shRNA@Fe_3O_4 MNPs +AMF treatment, and this result was consistent with the mechanism reported by Masayuki Hiraki et al[21] that MUC1-C promotes apoptosis in TNBC cells through the MUC1-C→NF-κBP65→BCL2A1 signaling pathway.

Ferroptosis is an iron- and reactive oxygen species (ROS)-dependent form of regulated cell death (RCD), and iron accumulation and subsequent lipid peroxidation play an important role in the development of ferroptosis.[39] When intracellular iron ion-dependent ROS accumulate in excess, the cell's antioxidant capacity is reduced, such as the diminished scavenging of GPX4, a key transcription factor that regulates resistance to oxidative stress, which is an important regulator of intracellular redox homeostasis.[40] GPX4 dysregulates the homeostasis of ROS production and degradation, the cell membrane structure is disrupted, and the cell dies.[41] Irons and the various molecules and signals involved in iron metabolism and lipid peroxidation are critical in regulating ferroptosis. In living organisms, the maintenance of iron homeostasis is tightly regulated. Iron has two oxidation states, Fe^{2+} and Fe^{3+}. Fe^{3+} in food is reduced to Fe^{2+} in the intestine and absorbed by the epithelial cells of the small intestine. Fe^{2+} is transported extracellularly and oxidized to Fe^{3+} by the action of membrane iron transport proteins, which are bound to transferrin (TF) (serum transferrin or lactoferrin) to form the TF-Fe^{3+} complex and transported to various tissues and organs via the blood circulation. Fe^{3+} is bound to the transferrin receptor (TFRC) on the cell membrane and is reduced to Fe^{2+} by the metal reductase STEAP3, which then releases Fe^{2+} into the dynamic iron pool of the cytoplasm via divalent metal transporter protein 1. The excess iron is stored in the cell cytoplasm as ferritin light chain (FTL) and FTH1. Under normal physiological conditions, the dynamic iron pool maintains iron homeostasis. When Fe^{2+} is abnormally increased and pooled in the cell for various reasons (eg abnormal FTH1/FTL expression, dysfunction, or autophagic degradation), the Haber-Weiss reaction (Haber-Weiss) with Fenton reaction occurs, generating a large amount of ROS, which undergoes a series of peroxidation reactions with the polyunsaturated fatty acid (PUFA) on the cell membrane, generating lipid peroxides that disrupt the cell membrane structure and cause cellular ferroptosis. MUC1-C is associated with the maintenance of glutathione (GSH) levels and redox homeostasis. According to other researchers' reports, both MUC1-C shRNA and Fe_3O_4 MNPs can induce ferroptosis in tumor cells. For example, Hasegawa et al[42] confirmed that inhibition of MUC1-C was able to induce ferroptosis in TNBC through the MUC1-C/xCT (The xCT light chain of the cystine/glutamate transporter) signaling pathway, inhibiting MUC1-C-mediated TNBC cell self-renewal capacity and tumorigenicity. Xue et al[43] demonstrated that moderate heating and the synergistic effect of Fe_3O_4 NPs could trigger redox homeostasis of the tumor cells and induce ferroptosis. Meaningful evidence of ferroptosis was observed in our experimental group (Fe_3O_4-shRNA+AMF), which was associated with Fe^{2+} and heat-induced ferroptosis process and synergized with the mentioned above mechanism of inhibition of MUC1-C/xCT-induced ferroptosis (CI>1.0). Notably, we also observed that the expression of GPX4, NRF2, and FTH1 proteins, which are closely related to ferroptosis, were significantly inhibited in cells and tissues after MUC1-C shRNA@Fe_3O_4 MNPs +AMF treatment. It implies that the ferroptosis mechanism and ferroptosis-associated tumor signal pathways may be activated.[44] In general, it is speculated that with the AMF conditions, the MUC1-C shRNA@Fe_3O_4 MNPs induce apoptosis and improve therapeutic sensitivity through MUC1-C-mediated signal pathways, and then induce ferroptosis by increasing the Fe^{2+} and temperature, finally, destroy the heterogeneous tumor cells through magnetic-hyperthermia therapy.

Conclusion

In conclusion, we successfully prepared MUC1-C shRNA@Fe_3O_4 MNPs with both magnetic thermotherapy and gene therapy functions. It can target MUC1-C for specific gene therapy of TNBC, and overcome the spatiotemporal heterogeneity of tumors by generating non-specific tumor therapeutic effects through LRMH in AMF, thus effectively inhibiting the proliferation, migration, and invasion of TNBC. Given the abilities of their gene therapy and hyperthermia therapy abilities, as well as the remarkable combined effectiveness and biosafety in AMF, MUC1-C shRNA@Fe_3O_4 MNPs might be a potential candidate to improve the treatment result of TNBC, especially MUC1-positive TNBC.

Acknowledgments

This research was supported by the Natural Science Foundation of Nanjing University of Chinese Medicine, China (XZR2020093), Taizhou People's Hospital Medical Innovation Team Foundation (CXTDA201901), and the 333 Plan Foundation of Jiangsu, China (Jiangsu Talent Office [2022] 21-2). Thanks to the Laboratory Animal Center of Nantong University for providing convenience in this research. Dr. Shuangshuang Wang, Department of Pathology, Affiliated Hospital of Nanjing University of Traditional Chinese Medicine, also contributed to this article (in pathological detection and judgment).

Disclosure

The authors declare no conflicts of interest in this work.

References

1. Siegel RL, Miller KD, Fuchs HE, Jemal A. Cancer statistics, 2022. *CA Cancer J Clin*. 2022;72(1):7–33. doi:10.3322/caac.21708
2. Howard FM, Olopade OI. Epidemiology of triple-negative breast cancer: a review. *Cancer J*. 2021;27(1):8–16. doi:10.1097/PPO.0000000000000500
3. Rugo HS, Olopade OI, DeMichele A, et al. Adaptive randomization of veliparib-carboplatin treatment in breast cancer. *N Engl J Med*. 2016;375(1):23–34. doi:10.1056/NEJMoa1513749
4. Schmid P, Cortes J, Dent R, et al. Event-free survival with pembrolizumab in early triple-negative breast cancer. *N Engl J Med*. 2022;386(6):556–567. doi:10.1056/NEJMoa2112651
5. Downs-Canner S, Mittendorf EA. Preoperative immunotherapy combined with chemotherapy for triple-negative breast cancer: perspective on the KEYNOTE-522 study. *Ann Surg Oncol*. 2023;30(6):3166–3169. doi:10.1245/s10434-023-13267-z
6. Shastry M, Jacob S, Rugo HS, Hamilton E. Antibody-drug conjugates targeting TROP-2: clinical development in metastatic breast cancer. *Breast*. 2022;66:169–177. doi:10.1016/j.breast.2022.10.007
7. Chen W, Zhang Z, Zhang S, Zhu P, Ko JK, Yung KK. MUC1: structure, function, and clinic application in epithelial cancers. *Int J Mol Sci*. 2021;22(12):6567. doi:10.3390/ijms22126567
8. Li Z, Yang D, Guo T, Lin M. Advances in MUC1-mediated breast cancer immunotherapy. *Biomolecules*. 2022;12(7):952. doi:10.3390/biom12070952
9. Kufe DW. MUC1-C oncoprotein as a target in breast cancer: activation of signaling pathways and therapeutic approaches. *Oncogene*. 2013;32(9):1073–1081. doi:10.1038/onc.2012.158
10. Jing X, Liang H, Hao C, Yang X, Cui X. Overexpression of MUC1 predicts poor prognosis in patients with breast cancer. *Oncol Rep*. 2019;41(2):801–810. doi:10.3892/or.2018.6887
11. Kufe DW. MUC1-C in chronic inflammation and carcinogenesis; emergence as a target for cancer treatment. *Carcinogenesis*. 2020;41(9):1173–1183. doi:10.1093/carcin/bgaa082
12. Yamashita N, Kufe D. Addiction of cancer stem cells to MUC1-C in triple-negative breast cancer progression. *Int J Mol Sci*. 2022;23(15):8219. doi:10.3390/ijms23158219
13. Rajabi H, Hata T, Li W, et al. MUC1-C represses the RASSF1A tumor suppressor in human carcinoma cells. *Oncogene*. 2019;38(47):7266–7277. doi:10.1038/s41388-019-0940-1
14. Yamashita N, Morimoto Y, Fushimi A, et al. MUC1-C dictates PBRM1-mediated chronic induction of interferon signaling, DNA damage resistance, and immunosuppression in triple-negative breast cancer. *Mol Cancer Res*. 2023;21(3):274–289. doi:10.1158/1541-7786.MCR-22-0772
15. Yamashita N, Fushimi A, Morimoto Y, et al. Targeting MUC1-C suppresses chronic activation of cytosolic nucleotide receptors and STING in triple-negative breast cancer. *Cancers*. 2022;14(11):2580. doi:10.3390/cancers14112580
16. Yamashita N, Long M, Fushimi A, et al. MUC1-C integrates activation of the IFN-γ pathway with suppression of the tumor immune microenvironment in triple-negative breast cancer. *J Immunother Cancer*. 2021;9(1):e002115. doi:10.1136/jitc-2020-002115
17. Kufe DW. Chronic activation of MUC1-C in wound repair promotes progression to cancer stem cells. *J Cancer Metastasis Treat*. 2022;8:12. doi:10.20517/2394-4722.2022.03
18. Maeda T, Hiraki M, Jin C, et al. MUC1-C induces PD-L1 and immune evasion in triple-negative breast cancer. *Cancer Res*. 2018;78(1):205–215. doi:10.1158/0008-5472.CAN-17-1636
19. Hata T, Rajabi H, Takahashi H, et al. MUC1-C activates the NuRD complex to drive dedifferentiation of triple-negative breast cancer cells. *Cancer Res*. 2019;79(22):5711–5722. doi:10.1158/0008-5472.CAN-19-1034

20. Hata T, Rajabi H, Yamamoto M, et al. Targeting MUC1-C inhibits TWIST1 signaling in triple-negative breast cancer. *Mol Cancer Ther*. 2019;18(10):1744–1754. doi:10.1158/1535-7163.MCT-19-0156
21. Hiraki M, Maeda T, Mehrotra N, et al. Targeting MUC1-C suppresses BCL2A1 in triple-negative breast cancer. *Signal Transduct Target Ther*. 2018;3:13. doi:10.1038/s41392-018-0013-x
22. Bhattacharya A, Fushimi A, Yamashita N, et al. MUC1-C dictates JUN and BAF-mediated chromatin remodeling at enhancer signatures in cancer stem cells. *Mol Cancer Res*. 2022;20(4):556–567. doi:10.1158/1541-7786.MCR-21-0672
23. Borri F, Granaglia A. Pathology of triple negative breast cancer. *Semin Cancer Biol*. 2021;72:136–145. doi:10.1016/j.semcancer.2020.06.005
24. Yi GY, Kim MJ, Kim HI, Park J, Baek SH. Hyperthermia treatment as a promising anti-cancer strategy: therapeutic targets, perspective mechanisms and synergistic combinations in experimental approaches. *Antioxidants*. 2022;11(4):625. doi:10.3390/antiox11040625
25. Dias AMM, Courteau A, Bellaye PS, et al. Superparamagnetic iron oxide nanoparticles for immunotherapy of cancers through macrophages and magnetic hyperthermia. *Pharmaceutics*. 2022;14(11):2388. doi:10.3390/pharmaceutics14112388
26. De-Colle C, Beller A, Gani C, et al. Radiotherapy and hyperthermia for breast cancer patients at high risk of recurrence. *Int J Hyperthermia*. 2022;39(1):1010–1016. doi:10.1080/02656736.2022.2103593
27. Peeters H, van Zwol EM, Brancato L, MCdC MG, Bogers J. Systematic review of the registered clinical trials for oncological hyperthermia treatment. *Int J Hyperthermia*. 2022;39(1):806–812. doi:10.1080/02656736.2022.2076292
28. Chia BSH, Ho SZ, Tan HQ, Chua MLK, Tuan JKL. A review of the current clinical evidence for loco-regional moderate hyperthermia in the adjunct management of cancers. *Cancers*. 2023;15(2):346. doi:10.3390/cancers15020346
29. Chen Y, Zhou F, Wang C, Hu L, Guo P. Nanostructures as photothermal agents in tumor treatment. *Molecules*. 2022;28(1):277. doi:10.3390/molecules28010277
30. Cheng Z, Li M, Dey R, Chen Y. Nanomaterials for cancer therapy: current progress and perspectives. *J Hematol Oncol*. 2021;14(1):85. doi:10.1186/s13045-021-01096-0
31. Zhang L, Zhang Q, Hinojosa DT, et al. Multifunctional magnetic nanoclusters can induce immunogenic cell death and suppress tumor recurrence and metastasis. *ACS Nano*. 2022;16(11):18538–18554. doi:10.1021/acsnano.2c06776
32. Dou JP, Zhou QF, Liang P, Yu J. Advances in nanostructure-mediated hyperthermia in tumor therapies. *Curr Drug Metab*. 2018;19(2):85–93. doi:10.2174/1389200219666180129141757
33. Karvelas EG, Lampropoulos NK, Benos LT, Karakasidis T, Sarris IE. On the magnetic aggregation of Fe(3)O(4) nanoparticles. *Comput Methods Programs Biomed*. 2021;198:105778. doi:10.1016/j.cmpb.2020.105778
34. Fan R, Chen C, Mu M, et al. Engineering MMP-2 activated nanoparticles carrying B7-H3 bispecific antibodies for ferroptosis-enhanced glioblastoma immunotherapy. *ACS Nano*. 2023;17(10):9126–9139. doi:10.1021/acsnano.2c12217
35. Li S, Chen Y, Ma R, Du Y, Han B. Cationic lipid-assisted nanoparticles for simultaneous delivery of CD47 siRNA and R848 to promote antitumor immune responses. *Front Pharmacol*. 2023;14:1142374. doi:10.3389/fphar.2023.1142374
36. Guo T, Zhu Y, Yue M, Wang F, Li Z, Lin M. The therapeutic effects of DDP/CD44-shRNA nanoliposomes in AMF on ovarian cancer. *Front Oncol*. 2022;12:811783. doi:10.3389/fonc.2022.811783
37. Hernandes EP, Lazarin-Bidóia D, Bini RD, Nakamura CV, Cótica LF, de Oliveira Silva Lautenschlager S. Doxorubicin-loaded iron oxide nanoparticles induce oxidative stress and cell cycle arrest in breast cancer cells. *Antioxidants*. 2023;12(2):237. doi:10.3390/antiox12020237
38. Chauhan M, Basu SM, Qasim M, Giri J. Polypropylene sulphide coating on magnetic nanoparticles as a novel platform for excellent biocompatible, stimuli-responsive smart magnetic nanocarriers for cancer therapeutics. *Nanoscale*. 2023;15(16):7384–7402. doi:10.1039/D2NR05218K
39. Lei G, Zhuang L, Gan B. Targeting ferroptosis as a vulnerability in cancer. *Nat Rev Cancer*. 2022;22(7):381–396. doi:10.1038/s41568-022-00459-0
40. Yang WS, SriRamaratnam R, Welsch ME, et al. Regulation of ferroptotic cancer cell death by GPX4. *Cell*. 2014;156(1–2):317–331. doi:10.1016/j.cell.2013.12.010
41. Zhang C, Liu X, Jin S, Chen Y, Guo R. Ferroptosis in cancer therapy: a novel approach to reversing drug resistance. *Mol Cancer*. 2022;21(1):47. doi:10.1186/s12943-022-01530-y
42. Hasegawa M, Takahashi H, Rajabi H, et al. Functional interactions of the cystine/glutamate antiporter, CD44v and MUC1-C oncoprotein in triple-negative breast cancer cells. *Oncotarget*. 2016;7(11):11756–11769. doi:10.18632/oncotarget.7598
43. Xie S, Sun W, Zhang C, et al. Metabolic control by heat stress determining cell fate to ferroptosis for effective cancer therapy. *ACS Nano*. 2021;15(4):7179–7194. doi:10.1021/acsnano.1c00380
44. Chen X, Kang R, Kroemer G, Tang D. Broadening horizons: the role of ferroptosis in cancer. *Nat Rev Clin Oncol*. 2021;18(5):280–296. doi:10.1038/s41571-020-00462-0